Design and Development of an Electronic Interface for Acquiring Signals from a Piezoelectric Sensor for Ultrasound Image Reconstruction

Elizabeth Espitia-Romero , Adriana Guzmán-López , Micael Gerardo Bravo-Sánchez * , Juan José Martínez-Nolasco , José Alfredo Padilla-Medina , Francisco Villaseñor-Ortega

Posted Date: 7 May 2025

doi: 10.20944/preprints202505.0430.v1

Keywords: Ultrasound; interface; piezoelectric sensor; analog filter; image reconstruction

 doi:10.20944/preprints202505.0430.v1

Article

Design and Development of an Electronic Interface for Acquiring Signals from a Piezoelectric Sensor for Ultrasound Image Reconstruction

Elizabeth Espitia-Romero [1], Adriana Guzmán-López [2], Micael Gerardo Bravo-Sánchez [2,*], Juan José Martínez-Nolasco [3], José Alfredo Padilla-Medina [4] and Francisco Villaseñor-Ortega [2]

[1] Departamento de Posgrado e Investigación (DEPI), Tecnológico Nacional de México (TecNM), Instituto Tecnológico de Celaya (ITC), Celaya 38010, Guanajuato, México
[2] Departamento de Ingeniería Bioquímica e Ingeniería Ambiental, Tecnológico Nacional de México (TecNM), Instituto Tecnológico de Celaya (ITC), Celaya 38010, Guanajuato, México
[3] Departamento de Ingeniería Mecatrónica, Tecnológico Nacional de México (TecNM), Instituto Tecnológico de Celaya (ITC), Celaya 38010, Guanajuato, México
[4] Departamento de Ingeniería Electrónica, Tecnológico Nacional de México (TecNM), Instituto Tecnológico de Celaya (ITC), Celaya 38010, Guanajuato, México
* Correspondence: gerardo.bravo@itcelaya.edu.mx

Abstract: The increasing demand for accurate and accessible medical imaging has driven efforts to develop technologies that overcome limitations associated with conventional imaging techniques, such as MRI and CT scans. This study presents the design and implementation of an electronic interface for acquiring signals from a piezoelectric ultrasound sensor, aimed at improving image reconstruction quality by addressing electromagnetic interference and speckle noise, two major factors that degrade image fidelity. The proposed interface is installed between the ultrasound transducer and acquisition system, allowing real-time signal capture without altering the medical equipment's operation. Using a printed circuit board with 110-pin connectors, signals from individual piezoelectric elements were analyzed using an oscilloscope. Results showed that noise amplitudes occasionally exceed those of the acoustic echoes, potentially compromising image quality. By enabling direct observation of these signals, the interface facilitates the future development of analog filtering solutions to mitigate high-frequency noise before digital processing. This approach reduces reliance on computationally expensive digital filtering, offering a low-cost, real-time alternative. The findings underscore the potential of the interface to enhance diagnostic accuracy and support further innovation in medical imaging technologies.

Keywords: ultrasound; interface; piezoelectric sensor; analog filter; image reconstruction

1. Introduction

The generation of diagnostic images is a highly significant area of research in biomedicine. Currently, medical imaging plays a crucial role in the rapid diagnosis and monitoring of the progression of various diseases. Some of its most relevant applications include cancer detection, monitoring of changes in cancerous tissues, muscle injuries, evaluation of blood vessels, joint analysis, internal organ observation, fetal examination during pregnancy, kidney stone monitoring, physiotherapy assessment, and analysis of cosmetic surgeries [1–3]. Magnetic resonance imaging (MRI) [4], positron emission tomography (PET) [5], computed tomography (CT) [6,7], laser scanning confocal microscopy (LSCM) [8], photoacoustic imaging (PA) [9,10], and hybrid techniques such as MRI-PA, which have demonstrated excellent performance [11], are among the technologies that rely primarily on image interpretation. However, these methods are often limited by the need for exogenous contrast agents, exposure to radiation, and high costs. Developing reliable and accessible

 doi:10.20944/preprints202505.0430.v1

technologies to support medical diagnosis remains a constant challenge. Ultrasound imaging presents an attractive alternative, enabling faster and more accurate diagnoses. It does not require contrast agents and operates based on the principles of acoustic wave propagation through piezoelectric elements, electronics, and clinical research, to reconstruct images from ultrasonic signals [12,13]. These systems offer significant advantages: they utilize non-ionizing energy, are non-invasive, provide real-time data, and can represent images of both structural or anatomical dimensions (mm) and functional scales (μm) [14,15].

The study of acoustic waves is a research area of high interest. Currently, the literature presents various proposals based on physical principles that involve the generation of acoustic waves using pulsed laser light, such as for monitoring the elimination of nanoparticles in the kidneys of a live mouse [16]; detection and imaging of defects in metallic components [17]; image reconstruction of breast tissue for the detection of malignant lesions [18]; deep learning algorithms aimed at improving medical diagnoses through imaging using ultraviolet light in photoacoustic applications on thin human tissue samples [19]; and automatic classification of breast tumors in ultrasound imaging, showing improved diagnostic accuracy [20]. Additional applications include the detection of high-temperature points for fire prevention and control [21], classification of dehydrated strawberries and fruit ripeness using artificial neural networks [22], studies on human cadaver heads to identify optimal acoustic receiver locations for minimally invasive, image-guided neurosurgery [23], and acoustic waves applied to biodetection tasks such as cell manipulation and the quantification of proteins, vapor molecules, and DNA hybridizations [24,25]. Acoustic wave techniques have also been applied in the food industry, particularly in the development of food processing methods for cell destruction and intracellular material extraction. Ultrasonic processes can activate microorganisms and enzymes to preserve or decontaminate food, especially when ultrasound is combined with heat and high-pressure techniques [26]. Proposals aimed at improving the tangential resolution of systems with a finite number of sensors include multi-angle systems that rotate around the sample to subsequently generate the image [27]. Other studies highlight the importance of enhancing image reconstruction algorithms, such as SPANNER, which addresses artifact reduction through precise modeling [28], or the lag-based delay multiply and sum combined with coherence factor (DMAS-LAG-CF) algorithm, which improves resolution and contrast for distinguishing malignant from benign ovarian lesions [29]. Another technique, the Single Sensor Scan Synthetic Aperture Focusing Technique (SSC-SAFT), demonstrates the ability to eliminate sidelobe artifacts and comet tail artifacts [30]. A realistic ultrasound image simulation tool developed in MATLAB for educational and research purposes has also been introduced, named the Matlab UltraSound Toolbox (MUST) [31].

Similarly, other studies mention the two main categories of artifacts in acoustic imaging: those related to assumptions made by the ultrasound imaging system, and those caused by interference within the equipment. These artifacts can lead to incorrect diagnoses, as they obscure and degrade the quality of the resulting image [32,33]. To mitigate axial artifacts—typically located beneath the actual image and consisting of acoustic reverberations that prolong the wave travel time—image reconstruction algorithms have been implemented. One proposed approach involves signal restoration prior to applying conventional methods such as Delay-and-Sum (DAS) and Delay-Multiply-and-Sum (DMAS), demonstrating a 45% improvement in image resolution and contrast, and an 80% suppression of background artifacts [34]. Regarding artifacts caused by electromagnetic interference in the equipment, these are attributed to factors such as insufficient shielding, transducer operation issues, inadequate sampling frequency—which may induce aliasing artifacts—and the limited processing speed of image reconstruction algorithms. These types of interference result in speckle noise in ultrasound images, which degrades the visual quality and impairs accurate human interpretation by introducing a grainy pattern [35,36]. In [37], a comparative study was conducted on noise reduction methods to improve ultrasound image reconstruction of blood cells. The study examined low-pass, band-pass, and discrete wavelet transform (DWT)-based filters implemented using MATLAB's Signal Processing Toolbox and Wavelet Toolbox functions. Evaluation metrics such

 doi:10.20944/preprints202505.0430.v1

as Root Mean Square Error (RMSE), Signal-to-Noise Ratio (SNR), and Contrast-to-Noise Ratio (CNR) were used to assess performance.

Additionally, [38] presents a speckle noise removal proposal through a filtering algorithm applied directly to medical images, employing Speckle Reducing Anisotropic Diffusion (SRAD), Discrete Wavelet Transform (DWT) using symmetry characteristics, Weighted Guided Image Filtering (WGIF), and Gradient Domain Guided Image Filtering (GDGIF). The results showed effective speckle noise suppression while preserving the edge information of the imaged objects. Finally, [39] explores a study of twenty-seven techniques aimed at smoothing or eliminating speckle noise in ultrasound images. This study compared spatial filtering, diffusion filtering, wavelet filtering, and machine learning techniques focused on deep learning. Although classical and hybrid filtering methods provided accurate results in reducing noise and preserving information, they typically required manual parameter tuning, as their effectiveness depends heavily on the nature of the input data. On the other hand, machine learning techniques face limitations due to the difficulty of acquiring clean and representative training data, particularly in real-world clinical scenarios. It is therefore important to direct future research toward speckle noise filtering, with the goal of improving region-of-interest detection and developing methodologies that offer enhanced solutions to current challenges. For this reason, an analog filtering approach is proposed.

2. Electronic Interface Design

Ultrasound waves are produced by transducers activated at frequencies above 20 kHz, which is commonly accepted as the upper frequency limit of human hearing. Figure 1 shows a typical ultrasound hardware system, which mainly consists of a transducer, an ultrasonic pulse transmitter, a receiver, a logic control unit, a storage system, and a display unit [40].

The ultrasonic pulse transmitter comprises high-power MOSFETs, a logic controller, and a high-voltage power supply. The receiver is primarily composed of a Voltage-Controlled Amplifier (VCA) and an analog-to-digital converter. In our case, this system operates correctly and has been validated for medical applications in small animal species. However, the images generated still contain noise, complicating diagnosis due to difficulties in interpreting the images. Therefore, the electronic interface developed in this work aims to visualize signals directly from the transducer in real time, without any processing. The interface is placed immediately after the connection port between the transducer and the signal acquisition board within the ultrasound system's medical equipment. This connection point is indicated by the letter 'A' in Figure 1.

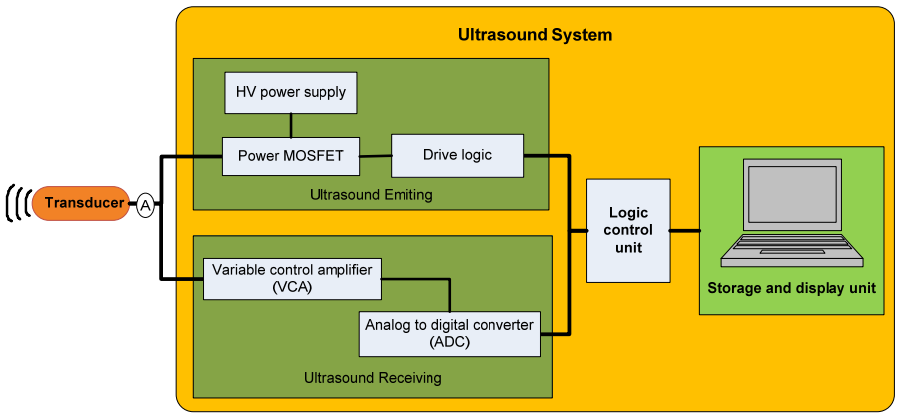

Figure 1. Diagram of the typical hardware system of an ultrasound equipment.

At point A in Figure 1, there is a convex-type transducer with 80 ceramic elements, known as piezoelectric materials, which convert acoustic energy into electrical signals and vice versa. When a voltage is applied to the piezoelectric element, the material undergoes expansion and/or contraction, thereby generating an acoustic signal [41,42]. The transducer at point A is connected to the medical

 doi:10.20944/preprints202505.0430.v1

ultrasound equipment, where the emission and reception of acoustic signals take place. The schematic shown in Figure 2 illustrates how the proposed electronic interface is connected, with the purpose of observing the experimental signals in real time without interfering with the operation of the medical device. As shown, the medical ultrasound system (a) is directly connected to the proposed electronic interface (b). This printed circuit board (PCB) is designed to connect in parallel with both the transducer (c) and the signal acquisition system or oscilloscope (d). The oscilloscope enables the acquired signals to be processed via a computer, allowing for the reconstruction of an alternative ultrasound image.

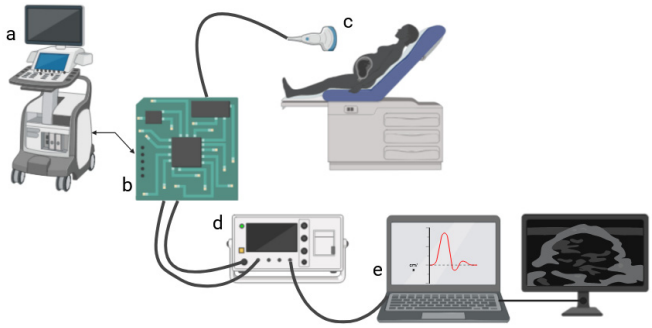

Figure 2. The proposed interconnection is shown, (a) medical ultrasound equipment, (b) proposed electronic interface, (c) transducer, (d) oscilloscope and (e) computer/monitor.

Initially, an inspection is conducted to understand the electronic configuration connecting the transducer to the ultrasound system. The transducer connection port on the equipment contains 110 pins which transmit electrical signals between components. For the design of the proposed electronic interface, it is essential to determine the pin configuration and the type of signals each pin carries. The design process began with the development of the printed circuit board (PCB) that constitutes the proposed electronic interface. This PCB features three 110-pin connectors and 220 laminated conductive tracks that provide interconnection between the ports. Figures 3 and 4 display the six layout layers, each showing the routing of approximately 36 tracks per layer for port interconnection. The tracks are evenly distributed, which is critical to ensure optimal performance and to avoid any signal distortion or interference with the medical ultrasound system due to electromagnetic incompatibility between components [43,44]. Table 1 presents the technical and manufacturing specifications of the PCB.

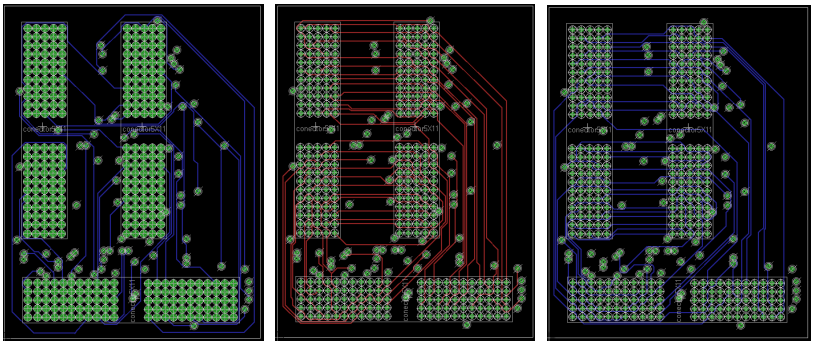

 doi:10.20944/preprints202505.0430.v1

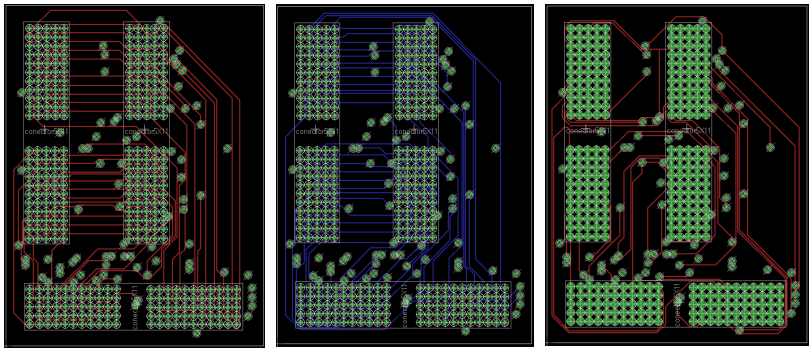

Figure 3. Interface board plans.

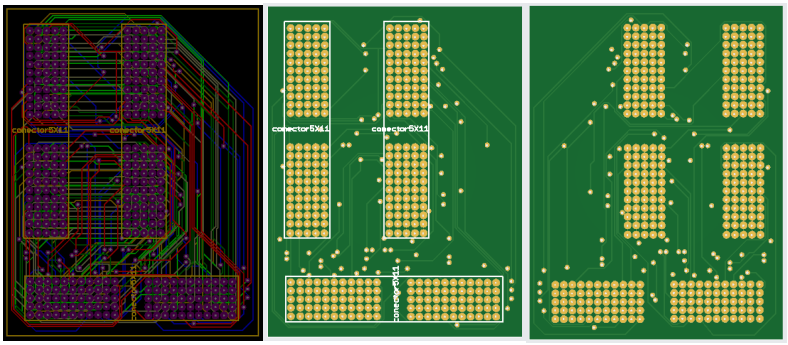

(**a**) (**b**) (**c**)

Figure 4. 2D view of (a) 6 planes with the 220 tracks, (b) top PCB and (c) bottom PCB of the proposed electronic interface.

Table 1. Electronic interface design data.

Parameter	Specification
Phenolic board material	Epoxy fiberglass
Maximum deformation temperature	130°C
Breakdown Voltage	3000V
Thermal Conductivity	1W/mK
Copper Weight	1 OZ
Color	Verde
Phenolic board dimensions	60 mm* 78 mm
Number of planes	6 planes
Plate thickness	1.6mm
Average number of tracks per plan	36
Inlet and outlet port dimensions	10mm*50mm

Subsequently, the installation of the terminals for the three CompactPCI (CPCI) ports—two female and one male, each with 110 pins—is carried out on the fabricated printed circuit board using commercially available solder composed of 60% tin and 40% lead. Figure 5 shows the PCB with the port terminals installed. Finally, the proposed electronic interface board is connected to the medical ultrasound system at the terminal that contains the transducer connection port.

 doi:10.20944/preprints202505.0430.v1

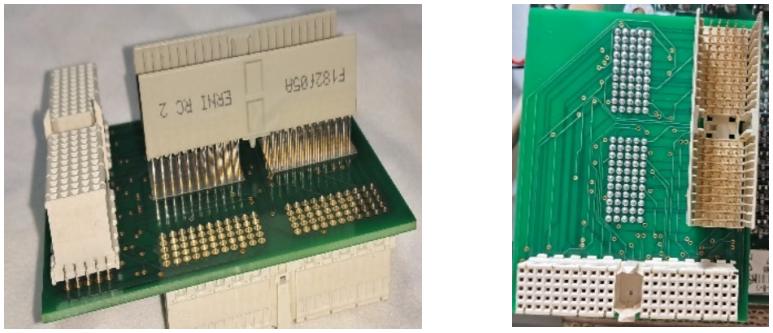

(**a**) (**b**)

Figure 5. Proposed electronic interface (a) prior to soldering and (b) with all three ports soldered.

The acquisition of signals through the electronic interface connected simultaneously to the ultrasound equipment and the transducer allows the observation and parallel acquisition of signals emitted and received by each of the piezoelectric elements in the transducer. To perform this process effectively, a stable environment is required to ensure proper intervention, including the preparation of a biological tissue emulator and the selection of an observation object. As the observation object, a 50-cent Mexican coin was selected. Its physical characteristics are shown in Figure 6. This coin has a diameter of 17 mm, a thickness of 1.9 mm, and a weight of 3.103 g. It features a reeded edge and is made of stainless steel. The composition of this stainless steel includes 16% chromium, 0.75% nickel, 0.12% carbon, 1% silicon, 1% manganese, 0.03% sulfur, 0.04% phosphorus, with the remaining percentage being iron [45].

To prepare a 400 mL biological tissue emulator gel, bacteriological agar is used. This type of agar is widely employed as a tissue-mimicking material due to its notable properties, including gelation at room temperature between 32°C and 38°C, a gel strength of 750 g/cm² which provides suitable firmness, chemical inertness, uniform distribution in gelled media, and ease of preparation [46].

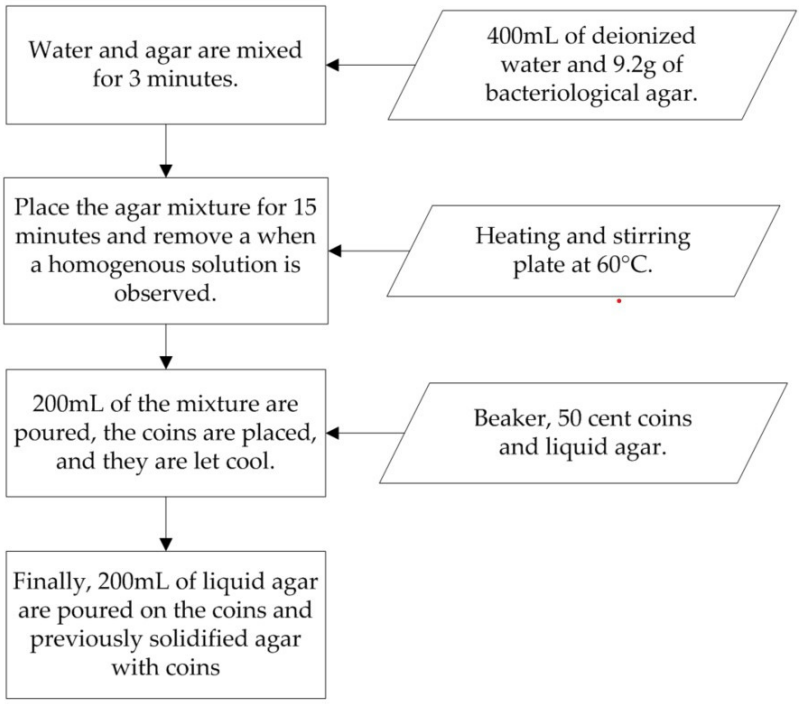

Figure 6. Process diagram for the development of a biological tissue emulator.

Figure 6 presents a diagram of the preparation method for 400 mL of agar-based gel. The procedure requires 400 mL of deionized water and powdered agar. Initially, 400 mL of deionized

 doi:10.20944/preprints202505.0430.v1

water and 9.2 g of agar are poured into a beaker. The water and agar are then mixed for approximately 3 minutes, after which the mixture is placed on a heating and stirring plate at 60°C for 15 minutes, or until a homogeneous solution is observed. From the homogeneous mixture, 200 mL are poured into a separate beaker and allowed to cool for 5 minutes at room temperature (25°C). Five coins are then positioned vertically in the solidified agar. The remaining liquid agar is poured over the beaker containing the embedded coins and left to cool for 5 minutes at room temperature, or alternatively, the beaker can be covered and refrigerated. Finally, the transducer of the ultrasound system is mounted on a universal stand above the prepared tissue emulator and adjusted until the coin images become visible on the ultrasound display.

3. Results

To evaluate the acquired signals, measurements were carried out using an oscilloscope connected to the port of the electronic interface positioned between the ultrasound system and the transducer. The oscilloscope used was a UNI-T UPO1202CS model, featuring a sampling rate of 1 GS/s. Among the 110 pins monitored on the electronic interface, 80 were identified as ultrasonic signal lines corresponding to each piezoelectric element in the transducer connected to the system. Additionally, 26 pins were identified as ground reference signals (GND), 2 pins carried 5 V DC signals, and 2 pins carried 3 V DC signals. Figure 7 illustrates the pin configuration of the electronic interface port, with each signal numbered consecutively to indicate its correspondence to the individual transducer elements (a) that comprise the ultrasound sensor (b) within the system.

5V	5V	1	3	6	11	GND	19	23	28	32		GND	40	44	48	52	GND	61	65	69	73	GND
GND	GND	2	4	7	GND	15	20	24	29	33		37	41	GND	49	53	57	62	66	70	GND	77
GND	3V	GND	GND	8	12	16	21	25	GND	34		38	42	45	GND	54	58	63	67	GND	74	78
GND	GND	GND	GND	9	13	17	22	26	30	35		GND	43	46	50	55	59	64	GND	71	75	79
3V	GND	GND	5	10	14	18	GND	27	31	36		39	GND	47	51	56	60	GND	68	72	76	80

(**a**)

(**b**)

Figure 7. Schematic of (a) distribution of the 110 signals at the interface port and (b) transducer with the distribution of the 80 piezoelectric elements.

Figure 7a shows the port that constitutes the electronic interface, in which the numbers corresponding to the piezoelectric transducers forming the sensor head are highlighted in green, the ground reference signals (GND) in yellow, and the DC voltage lines (5 V and 3 V) in white. The sensor head, depicted in Figure 7b, contains 80 piezoelectric elements arranged consecutively within the head, specifically in the insulating window that makes contact with the biological tissue emulator. These elements in Figure 7b correspond directly to the numbering indicated on the electronic interface in Figure 7a. Following the mapping of the piezoelectric elements and the electronic interface, all 110 signals were acquired from the interface in real-time, operating in parallel with the ultrasound system (including 80 ultrasound transmit-receive signals, 26 ground reference signals, and 4 direct current voltage lines). From the 80 ultrasonic signals, a representative subset of 30 signals was selected for image representation. These selected signals are displayed in Figures 8–10. The sensor ranges shown in these figures correspond to piezoelectric transducers numbered 1–10, 31–40, and 71–80, respectively.

 doi:10.20944/preprints202505.0430.v1

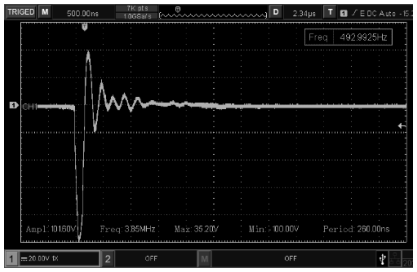

1

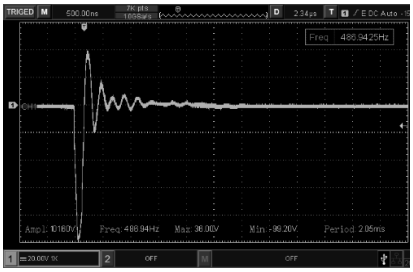

2

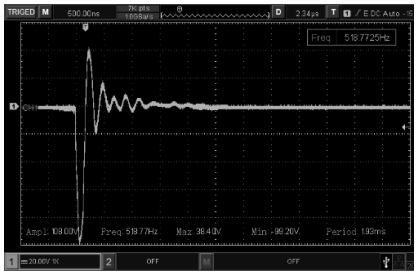

3

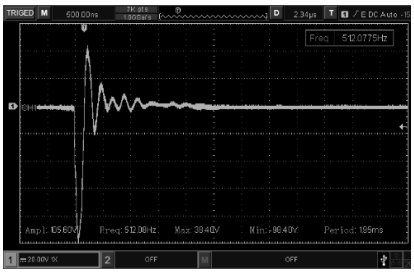

4

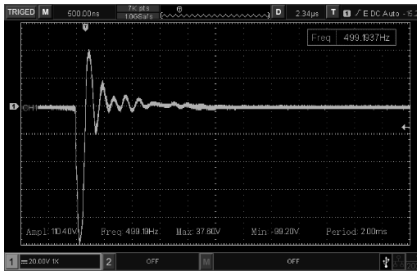

5

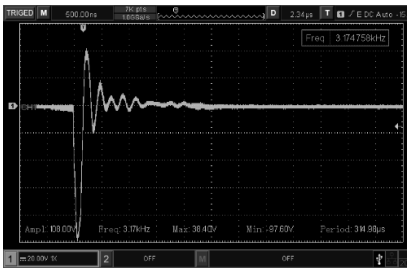

6

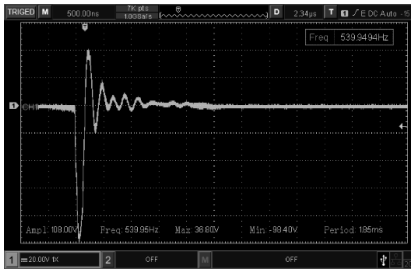

7

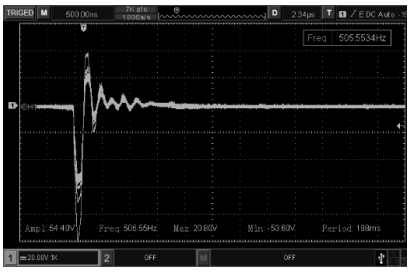

8

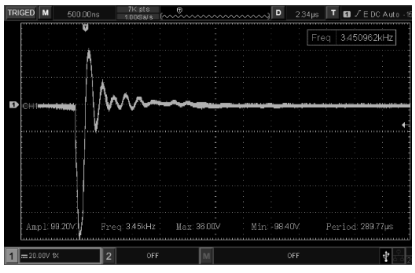

9

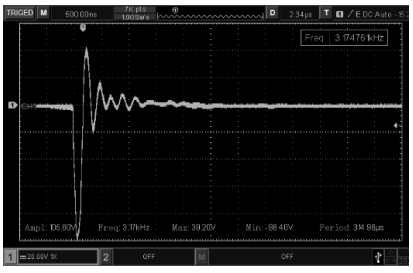

10

Figure 8. Acoustic signals from the piezoelectric sensor 1 to 10.

 doi:10.20944/preprints202505.0430.v1

Figure 8 shows the acquired signals corresponding to piezoelectric transducers numbered 1 through 10. These signals clearly exhibit both the transmission and the reception of the ultrasound echo. The measurements were obtained using a conventional probe with no attenuation adjustment, set at 20 Volts/div. The transmission pulses reached amplitudes of up to 150 Volts, while the echo signals displayed varying amplitudes at a frequency of 3.5 MHz. The amplitude of the echo signals ranged from approximately 200 mV to 1.84 V.

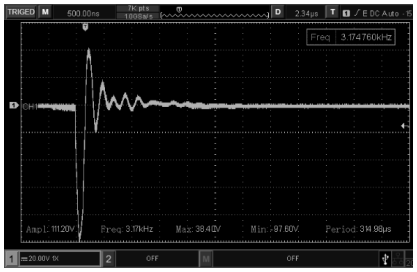

31

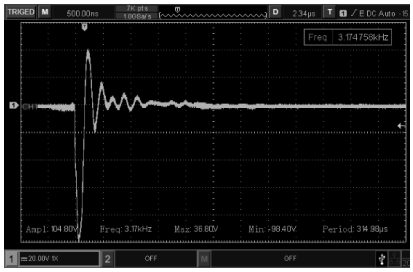

32

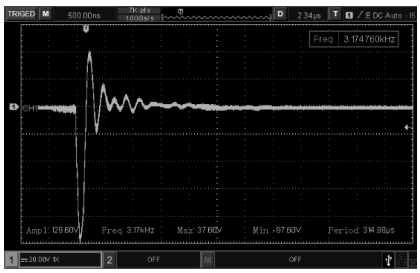

33

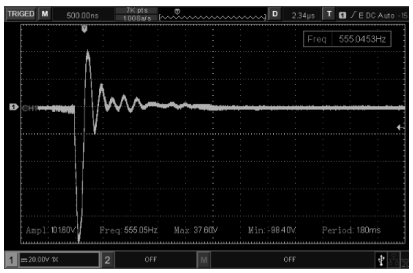

34

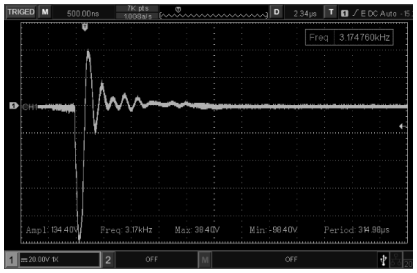

35

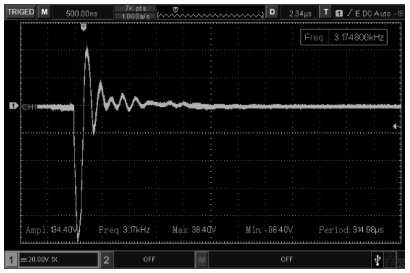

36

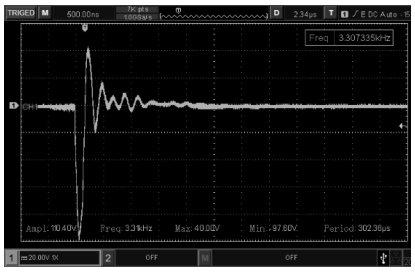

37

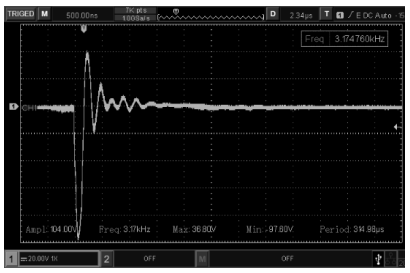

38

 doi:10.20944/preprints202505.0430.v1

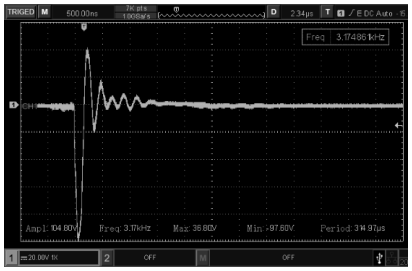

39

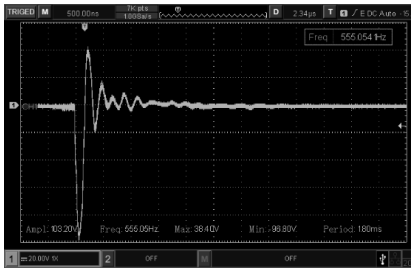

40

Figure 9. Acoustic signals from the piezoelectric sensor 31 to 40.

Figure 9 displays the acquired signals from piezoelectric transducers numbered 31 through 40. These signals show both the transmission and reception of ultrasound echoes. The measurements were taken using a conventional probe without attenuation adjustment, set at 20 Volts/div. The transmitted signals reached amplitudes of up to 150 Volts, while the echoes exhibited varying amplitudes at a frequency of 3.5 MHz. The amplitude of the echo signals ranged from approximately 400 mV to 1.6 V.

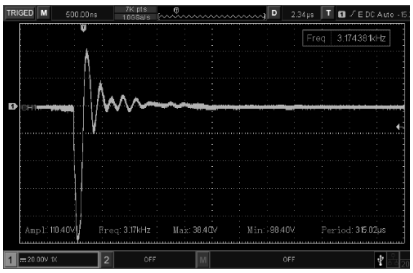

71

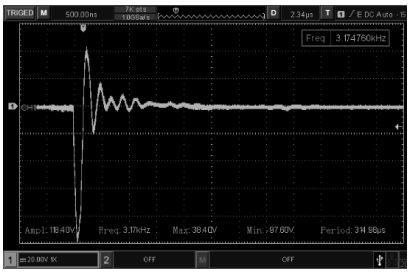

72

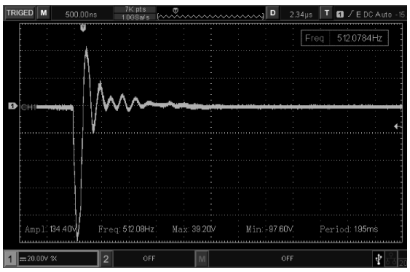

73

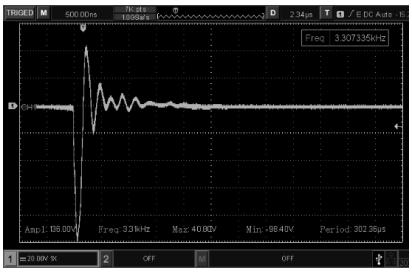

74

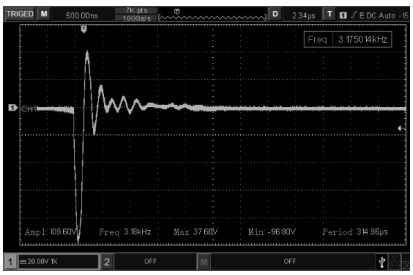

75

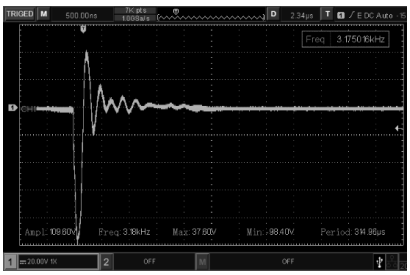

76

 doi:10.20944/preprints202505.0430.v1

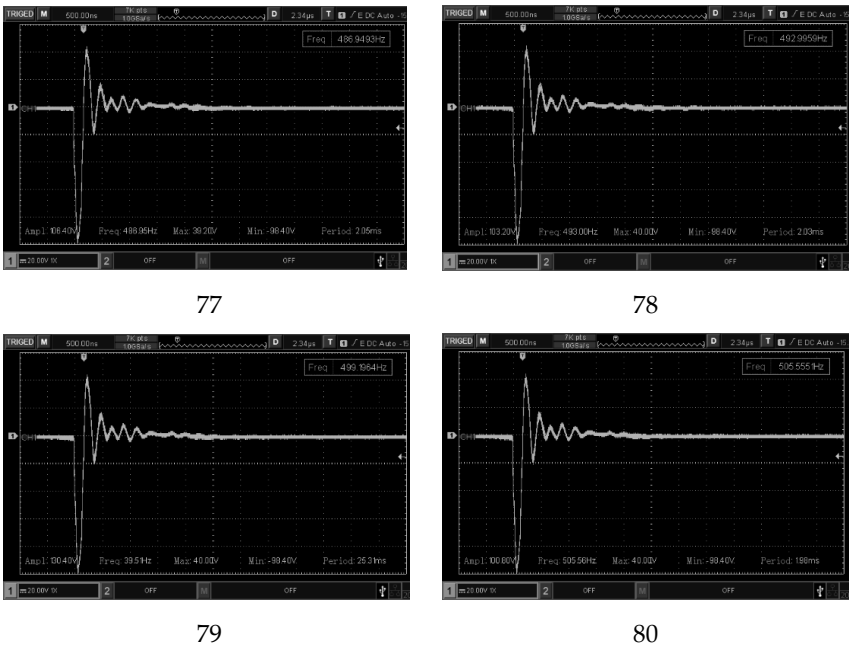

77 78

79 80

Figure 10. Acoustic signals from the piezoelectric sensor 71 to 80.

Likewise, Figure 9 shows the acquired signals corresponding to the piezoelectric transducers numbered 71 to 80, in which the emission and reception of the ultrasound signal echo can be observed. These signals were obtained using a conventional probe without attenuation adjustment, set at 20 Volts/div, displaying an emission amplitude of up to 150 Volts and varying echo amplitudes at a frequency of 3.5 MHz. The amplitude of the echoes from these signals' ranges from 250 mV to 1.9 V. To clearly observe the amplitude of the echoes, Figure 11 presents a zoomed-in view at the focal distance of the image obtained by the oscilloscope for the acoustic signal echo and a GND reference signal from the system.

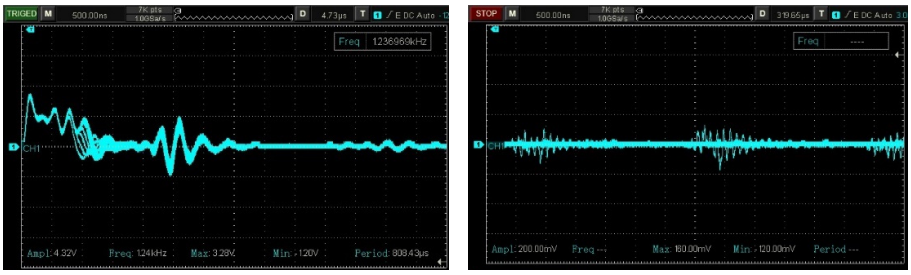

(**a**) (**b**)

Figure 11. Magnification at the focal distance of the image of a) acoustic signal number nine with the amplitude of the first and second echo and b) noise signal at GND.

Figure 11 shows a magnified view at the focal distance of the image obtained from Signal 9 using a conventional probe without attenuation adjustment, set at 2 Volts/div. In Figure 11a, it can be observed that the first echo has an amplitude of 1.8 V, while the second echo measures 400 mV. These low-amplitude echo signals are accompanied by high-frequency noise propagating through the ultrasound system's electronic circuitry. As depicted in Figure 11b, the noise signal was captured using a conventional probe without attenuation adjustment, set at 1 Volt/div. This GND signal illustrates how noise propagates within the system, with amplitudes ranging from 80 mV to 1.84 V. Low-amplitude echo signals combined with high-frequency noise are often either suppressed or amplified during signal processing via digital filtering algorithms. This process degrades image

 doi:10.20944/preprints202505.0430.v1

quality and simultaneously discards diagnostically relevant information for medical image reconstruction, ultimately reducing the effectiveness of timely medical diagnoses.

4. Discussion

This study presents a comprehensive investigation of current strategies for improving ultrasound image quality to ensure reliable medical diagnoses. Ultrasound technology has demonstrated widespread utility across diverse applications, including defect detection in metallic components, identification of high-temperature zones for fire prevention, fruit ripeness assessment, cadaver-guided neurosurgery, cancer and nanoparticle detection in murine models, and food decontamination. Compared to alternative imaging modalities such as magnetic resonance imaging (MRI), positron emission tomography (PET), computed tomography (CT), and photoacoustic imaging, ultrasound offers distinct advantages, particularly its cost-effectiveness and non-invasive nature due to the absence of ionizing radiation or contrast agents. Recent literature highlights significant advancements in image reconstruction algorithms, laser- and ultraviolet-induced acoustic wave generation, digital signal filtering techniques, and deep learning applications for direct medical image analysis. Given these technological advantages, broad applicability, and identified research opportunities, this study provides substantial value for advancing future medical diagnostics. Current limitations in accessing advanced transducer technologies, primarily due to their prohibitive costs, constrain both fundamental research and the development of improved image reconstruction strategies for optimized diagnoses. Our proposed electronic interface utilizes transducer technology from widely available commercial medical devices, thereby reducing research costs while enabling technological innovation in this field. A critical challenge in medical imaging involves addressing artifacts caused by electromagnetic interference, which degrade ultrasound image quality and diagnostic accuracy. These well-characterized artifacts, manifested as speckle noise, become embedded in acoustic signals through high-frequency interference between the wave generation system and piezoelectric transducers. Conventional approaches employ digital filters and reconstruction algorithms requiring substantial computational resources. However, concurrent processing of noise and acoustic signals may suppress relevant diagnostic information or amplify artifacts, potentially introducing false structures in reconstructed images and compromising diagnostic reliability - particularly when noise amplitudes (80 mV to 1.84 V) exceed expected echo signals. Our electronic interface facilitates enhanced understanding of acoustic phenomena in medical systems by enabling parallel signal observation without disrupting device operation. This system permits oscilloscope-based electronic signal analysis and real-time data acquisition, supporting image quality improvements through artifact reduction across various applications. Future work will focus on developing an analog filter for speckle noise elimination. Current digital filtering methods during image reconstruction not only degrade image quality but also demand excessive computational power. The proposed interface will enable parallel implementation of an analog filtering system, leveraging recent advancements in semiconductor technology that offer high-frequency operation, compact form factors, and cost efficiency. The principal advantage of analog filtering during acoustic signal emission-reception is real-time functional validation. This approach eliminates the need for additional computational processing during image reconstruction, as oscilloscope measurements directly assess filter performance with commercial transducers. This capability allows preliminary evaluation of the analog filter's noise suppression efficacy for high-frequency interference characteristics of medical ultrasound systems, prior to full computational system implementation.

5. Conclusions

This study underscores the critical need for enhancing ultrasound image quality through innovative approaches to optimize medical diagnoses. Ultrasound technology has proven to be remarkably versatile, with applications spanning multiple disciplines, while its advantages over

 doi:10.20944/preprints202505.0430.v1

alternative imaging modalities establish it as an indispensable tool in contemporary medicine. Nevertheless, electromagnetic interference and speckle noise persist as major challenges in image reconstruction. Our developed electronic interface facilitates real-time interference analysis and enables the implementation of efficient analog filtering. This approach could decrease dependence on expensive high-performance computing systems while improving medical image quality without loss of diagnostically relevant information. Implementing this technology promises not only more accurate diagnoses but also advances research in the field, paving the way for innovative solutions in medical imaging.

Author Contributions: Conceptualization, E.E.-R. and M.G.B.-S.; methodology, E.E.-R, M.G.B.-S., and A.G.-L.; software, E.E.-R., J.J.M.-N., and J.A.P.-M.; validation, J.A.P.-M.; formal analysis, M.G.B.-S., A.G.-L., J.J.M.-N., and F.V.-O.; investigation, E.E.-R. and M.G.B.-S.; resources, E.E.-R., A.G.-L., J.A.P.-M., F.V.-O., and E.E.-R.; writing—original draft preparation, E.E.-R., A.G.-L., and M.G.B.-S.; writing—review and editing, E.E.-R. and M.G.B.-S.; supervision, A.G.-L., J.A.P.-M., E.E.-R., and F.V.-O.; project administration, E.E.-R. and M.G.B.-S. All authors have read and agreed to the published version of the manuscript.

Funding: This research received no external funding.

Institutional Review Board Statement: Not applicable.

Informed Consent Statement: Not applicable.

Data Availability Statement: The original contributions presented in the study are included in the article.

Conflicts of Interest: The authors declare no conflicts of interest.

References

1. Malinowska, N.; Phang, S.; Seddon, A. B. Evolutionary Methods in Clinical Diagnostics. *21st International Conference on Transparent Optical Networks (ICTON)*, Angers, France, **2019**; pp. 1-4, https://doi.org/10.1109/ICTON.2019.8840440.
2. Amini, M.; Liu, P.; Umbaugh, S. E.; Marino, D. J.; Loughin, C. A. Thermographic image analysis method in detection of canine bone cancer (osteosarcoma). In *Proceedings of the 5th International Congress on Image and Signal Processing*, Chongqing, China, **2012**; pp 485–489. https://doi.org/10.1109/CISP.2012.6470012.
3. Panayides, A. S.; et al. AI in Medical Imaging Informatics: Current Challenges and Future Directions. *IEEE J. Biomed. Health Inform.* **2020**, *24* (7), 1837–1857. https://doi.org/10.1109/JBHI.2020.2991043.
4. Ladrova, M.; et al. Monitoring and Synchronization of Cardiac and Respiratory Traces in Magnetic Resonance Imaging: A Review. *IEEE Rev. Biomed. Eng.* **2022**, *15*, 200–221. https://doi.org/10.1109/RBME.2021.3055550.
5. Ghosh, K. K.; Padmanabhan, P.; Yang, C.-T.; Ng, D. C. E.; Palanivel, M.; Mishra, S.; Halldin, C.; Gulyás, B. Positron emission tomographic imaging in drug discovery. *Drug Discov. Today* **2022**, *27* (1), 280–291. https://doi.org/10.1016/j.drudis.2021.07.025.
6. Cao, W.; Wu, R.; Cao, G.; He, Z. A Comprehensive Review of Computer-Aided Diagnosis of Pulmonary Nodules Based on Computed Tomography Scans. *IEEE Access* **2020**, *8*, 154007–154023. https://doi.org/10.1109/ACCESS.2020.3018666.
7. Abdulbaqi, H. S.; Mutter, K. N.; Jafri, M. Z. M.; Al-Khafaji, Z. A. Estimation of brain tumour volume using expanded computed tomography scan images. In *Proceedings of the 23rd Iranian Conference on Biomedical Engineering and 1st International Iranian Conference on Biomedical Engineering (ICBME)*, Tehran, Iran, **2016**; pp 117–121. https://doi.org/10.1109/ICBME.2016.7890941.
8. Verveld, W.; de Wolf, J. R.; Legtenberg, C. G.; Knop, T.; Bosschaart, N. Human milk fat globule size distributions: Comparison between laser diffraction and 3D confocal laser scanning microscopy. *Food Res. Int.* **2024**, *198*, 115282. https://doi.org/10.1016/j.foodres.2024.115282.
9. Hakakzadeh, S.; Mozaffarzadeh, M. Multi-angle data acquisition to compensate transducer finite size in photoacoustic tomography. *Photoacoustics* **2022**, *27*, 100373. https://doi.org/10.1016/j.pacs.2021.100373.

 doi:10.20944/preprints202505.0430.v1

10. Steinberg, I.; Schneider, M. Superiorized Photo-Acoustic Non-Negative Reconstruction (SPANNER) for Clinical Photoacoustic Imaging. *IEEE Trans. Med. Imaging* **2021**, *40*, 1888–1897. https://doi.org/10.1109/TMI.2021.3062214.
11. Zhong, Y.; et al. Unsupervised Fusion of Misaligned PAT and MRI Images via Mutually Reinforcing Cross-Modality Image Generation and Registration. *IEEE Trans. Med. Imaging* **2024**, *43* (5), 1702–1714. https://doi.org/10.1109/TMI.2023.3347511.
12. Baun, J. Advances in Ultrasound Imaging Architecture: The Future Is Now. *J. Diagn. Med. Sonogr.* **2021**, *37* (3), 312–314. https://doi.org/10.1177/8756479321996274.
13. Tanter, M.; Fink, M. Ultrafast Imaging in Biomedical Ultrasound. *IEEE Trans. Ultrason. Ferroelectr. Freq. Control* **2014**, *61* (1), 102–119. https://doi.org/10.1109/TUFFC.2014.2882.
14. Wang, S.; Wang, X.; You, F.; Xiao, H. Review of Ultrasonic Particle Manipulation Techniques: Applications and Research Advances. *Micromachines* **2023**, *14*, 1487. https://doi.org/10.3390/mi14081487.
15. Xu, Y.; Wang, Y.; Yuan, J.; Cheng, Q.; Wang, X.; Carson, P. L. Medical Breast Ultrasound Image Segmentation by Machine Learning. *Ultrasonics* **2019**, *91*, 1–9. https://doi.org/10.1016/j.ultras.2018.07.006.
16. Jiang, X.; Du, B. Photoacoustic Imaging of Nanoparticle Transport in the Kidneys at High Temporal Resolution. *Angew. Chem.*, **2019**, *131*, 1–8.
17. Choi, S.; Young, K. Internal Defect Detection Using Laser-Generated Longitudinal Waves in Ablation Regime. *J. Mech. Sci. Technol.* **2018**, *32*, 4192–4200.
18. Nyayapathi, N.; Xia, J. Photoacoustic Imaging of Breast Cancer: A Mini Review of System Design and Image Features. *J. Biomed. Opt.* **2019**, *24*, https://doi.org/10.1016/j.pacs.2021.100308..
19. Kang, L.; Li, X.; Zhang, Y.; Wong, T. T. W. Deep Learning Enables Ultraviolet Photoacoustic Microscopy Based Histological Imaging with Near Real-Time Virtual Staining. *Photoacoustics* **2022**, *25*, 100308. https://doi.org/10.1016/j.pacs.2021.100308.
20. Chowdary, J.; Yogarajah, P.; Chaurasia, P.; Guruviah, V. A Multi-Task Learning Framework for Automated Segmentation and Classification of Breast Tumors from Ultrasound Images. *Ultrason. Imaging* **2022**, *44* (1), 3–12. https://doi.org/10.1177/01617346221075769.
21. Deng, J.; Qu, G.; Ren, S.; et al. Experimental Study on Acoustic Wave Propagation Characteristics and Main Paths in Loose Coal. *J. China Coal Soc.* **2023**, *48* (3), 1238–1245.
22. Przybył, K.; Duda, A.; Koszela, K.; Stangierski, J.; Polarczyk, M.; Gierz, Ł. Classification of Dried Strawberry by the Analysis of the Acoustic Sound with Artificial Neural Networks. *Sensors* **2020**, *20* (2), 499. https://doi.org/10.3390/s20020499.
23. Graham, M.; Huang, J. Simulations and Human Cadaver Head Studies to Identify Optimal Acoustic Receiver Locations for Minimally Invasive Photoacoustic-Guided Neurosurgery. *Photoacoustics* **2020**, *19*, 100180.
24. Huang, Y.; Das, P. K.; Bhethanabotla, V. R. Surface Acoustic Waves in Biosensing Applications. *Sens. Actuators Rep.* **2021**, *3*, 100041. https://doi.org/10.1016/j.snr.2021.100041.
25. Mandal, D.; Banerjee, S. Surface Acoustic Wave (SAW) Sensors: Physics, Materials, and Applications. *Sensors* **2022**, *22* (3), 820. https://doi.org/10.3390/s22030820.
26. Gallo, M.; Ferrara, L.; Naviglio, D. Application of Ultrasound in Food Science and Technology: A Perspective. *Foods* **2018**, *7* (10), 164. https://doi.org/10.3390/foods7100164.
27. Hakakzadeh, S.; Mozaffarzadeh, M. Multi-Angle Data Acquisition to Compensate Transducer Finite Size in Photoacoustic Tomography. *Photoacoustics* **2022**, *27*, 100373.
28. Steinberg, I.; Schneider, M. Superiorized Photo-Acoustic Non-Negative Reconstruction (SPANNER) for Clinical Photoacoustic Imaging. *IEEE Trans. Med. Imaging* **2021**, *40*, 1888–1897.
29. Yang, G.; Amidi, E. Photoacoustic Tomography Reconstruction Using Lag-Based Delay Multiply and Sum with a Coherence Factor Improves In Vivo Ovarian Cancer Diagnosis. *Biomed. Opt. Express* **2021**, *12*, 2250–2263.
30. Ruiz-Veloz, M.; Gutiérrez-Juárez, G.; Polo-Parada, L.; Cortalezzi, F.; Kline, D. D.; Dantzler, H. A.; Cruz-Alvarez, L.; Castro-Beltrán, R.; Hidalgo-Valadez, C. Image Reconstruction Algorithm for Laser-Induced Ultrasonic Imaging: The Single Sensor Scanning Synthetic Aperture Focusing Technique. *J. Acoust. Soc. Am.* **2023**, *153* (1), 560–572. https://doi.org/10.1121/10.0016996.

 doi:10.20944/preprints202505.0430.v1

31. Garcia, D. SIMUS: An Open-Source Simulator for Medical Ultrasound Imaging. Part I: Theory & Examples. *Comput. Methods Programs Biomed.* **2022**, *218*, 106726. https://doi.org/10.1016/j.cmpb.2022.106726.
32. Quien, M. M.; Saric, M. Ultrasound Imaging Artifacts: How to Recognize Them and How to Avoid Them. *Echocardiography* **2018**. https://doi.org/10.1111/echo.14116.
33. Claudon, M.; Bergès, O. Artifacts in Ultrasound. In *Echography of the Eye and Orbit*; Bergès, O., Ed.; Springer: Cham, **2024**. https://doi.org/10.1007/978-3-031-41467-1_6.
34. Hakakzadeh, S.; Amjadian, M.; Zhang, Y.; Mostafavi, S.; Kavehvash, Z.; Wang, L. Signal Restoration Algorithm for Photoacoustic Imaging Systems. *Biomed. Opt. Express* **2023**, *14*, 651–666.
35. Kremkau, F. W.; Taylor, K. J. Artifacts in Ultrasound Imaging. *J. Ultrasound Med.* **1986**, *5* (4), 227–237. https://doi.org/10.7863/jum.1986.5.4.227.
36. Huber, M. T.; Flint, K. M.; McNally, P. J.; Ellestad, S. C.; Trahey, G. E. Human Observer Sensitivity to Temporal Noise During B-Mode Ultrasound Scanning: Characterization and Imaging Implications. *Ultrason. Imaging* **2024**, *46* (3), 151–163. https://doi.org/10.1177/01617346241236160.
37. Guney, G.; Uluc, N.; Demirkiran, A.; Aytac-Kipergil, E.; Unlu, M. B.; Birgul, O. Comparison of Noise Reduction Methods in Photoacoustic Microscopy. *Comput. Biol. Med.* **2019**, *109*, 333–341. https://doi.org/10.1016/j.compbiomed.2019.04.035.
38. Choi, H.; Jeong, J. Despeckling Algorithm for Removing Speckle Noise from Ultrasound Images. *Symmetry* **2020**, *12* (6), 938. https://doi.org/10.3390/sym12060938.
39. Duarte-Salazar, C. A.; Castro-Ospina, A. E.; Becerra, M. A.; Delgado-Trejos, E. Speckle Noise Reduction in Ultrasound Images for Improving the Metrological Evaluation of Biomedical Applications: An Overview. *IEEE Access* **2020**, *8*, 15983–15999. https://doi.org/10.1109/ACCESS.2020.2967178.
40. Rodríguez-Olivares, N. A.; Cruz-Cruz, J. V.; Gómez-Hernández, A.; Hernández-Alvarado, R.; Nava-Balanzar, L.; Salgado-Jiménez, T.; Soto-Cajiga, J. A. Improvement of Ultrasonic Pulse Generator for Automatic Pipeline Inspection. *Sensors* **2018**, *18* (9), 2950. https://doi.org/10.3390/s18092950.
41. Bushberg, J. T.; Seibert, J. A.; Leidholdt, E. M.; Boone, J. M. *The Essential Physics of Medical Imaging*, 3rd ed.; Lippincott Williams & Wilkins: Philadelphia, **2011**.
42. Mahesh, M. The Essential Physics of Medical Imaging, Third Edition. *Med. Phys.* **2013**, *40* (7). https://doi.org/10.1118/1.4811156.
43. Balcells, J. *Interferencias Electromagnéticas en Sistemas Electrónicos*; Marcombo: Barcelona, **1991**.
44. Veraguas, J. P. L. *Compatibilidad Electromagnética y Seguridad Funcional en Sistemas Electrónicos*; Marcombo: Barcelona, 2010.
45. Banco de México. Moneda de 50 centavos de la familia D, circulación. https://www.banxico.org.mx (accessed 2025-04-29).
46. Palma-Chavez, J.; Wear, K. A.; Mantri, Y.; Jokerst, J. V.; Vogt, W. C. Photoacoustic Imaging Phantoms for Assessment of Object Detectability and Boundary Buildup Artifacts. *Photoacoustics* **2022**, *26*, 100348. https://doi.org/10.1016/j.pacs.2022.100348.